


Fundamental Limiting Efficiency and Intrinsic Loss Components of Quantum-Wire Intermediate-Band Solar Cells

Zahra Arefinia^{1,*} and Dip Prakash Samajdar²

¹Department of Photonics, Faculty of Physics, University of Tabriz, Tabriz, 51666-14766, Iran

²Department of Electronics and Communication Engineering, Pandit Dwarka Prasad Mishra Indian Institute of Information Technology, Design and Manufacturing, Jabalpur, Madhya Pradesh, 482005, India

 (Received 29 August 2020; revised 30 October 2020; accepted 23 November 2020; published 21 December 2020)

Quantum-wire intermediate-band solar cells (QW IBSCs) are good candidates for breaking the Shockley-Queisser limit; however, there are a few studies of them. In this paper, we derive the fundamental limiting efficiency (FLE), the theoretical upper limit of the power-conversion efficiency, for QW IBSCs by calculation of the intrinsic loss. To achieve this, based on a photon-electron detailed-balance principle, the intrinsic loss components (ILCs) are modeled in the QW IBSCs by our considering photon absorption and emission for two transverse directions of confined carriers and for a longitudinal direction of free carriers in the QWs. Furthermore, the ILCs and FLE are investigated in an experimental reported structure of an $\text{In}_x\text{Ga}_{1-x}\text{As}/\text{GaAs}$ QW IBSC. For this purpose, the two-dimensional Schrödinger equation and the Bloch approximation are used to obtain the placement and width of the intermediate band, respectively. Besides, the effect of changing the indium content, the diagonal length, and the period of QWs, which is a way to engineer the placement and width of the intermediate band and consequently the ILCs and FLE, on the FLE of $\text{In}_x\text{Ga}_{1-x}\text{As}/\text{GaAs}$ QW IBSCs is examined.

DOI: [10.1103/PhysRevApplied.14.064061](https://doi.org/10.1103/PhysRevApplied.14.064061)

I. INTRODUCTION

Various device concepts have been developed to theoretically design solar cells (SCs) with power-conversion efficiency (PCE) beyond the PCE of conventional single-junction SCs obtained by Shockley and Queisser [1]. These include multijunctions [2–5], up-conversion or down-conversion [6–9], multiple-exciton generation [10], spectral splitting [11,12], hot-carrier SCs [13,14], and intermediate-band (IB) SCs (IBSCs) [15–22]. IBSCs can use a highly ordered quantum-dot (QD) array in the intrinsic region of p - i - n SCs to introduce one IB [23,24] or two IBs [25,26] into the band gap of an intrinsic semiconductor to absorb photons with sub-band-gap energies. Use of a periodic array of quantum wires (QWs) in place of QDs has also been reported [27–32] due to some advantages of QWs over QDs, such as absorption of a broader range of the solar spectrum because of their higher density of states [33–35], more appropriate lifetime of photogenerated carriers [36], and increased photocurrent density in the plane of QWs [37,38]. An increase in the PCE of an $\text{In}_x\text{Ga}_{1-x}\text{As}/\text{GaAs}$ QW IBSC due to an increase in short-circuit current, resulting from sequential absorption of photons via the IB, was reported by Kunets *et al.* [27]. In QW IBSCs as QD IBSCs, the IB created by embedded QWs in a host semiconductor allows the absorption of

photons with energies less than the band gap of the host semiconductor leading to the more efficiently harvesting of the broadband solar spectrum, however, there are some differences between the mechanism of QW IBSCs and QD IBSCs resulting from confinement of carrier wave functions by QWs in two directions, not in three directions as in QDs. Therefore, the fundamental limiting efficiency (FLE), the theoretical upper limit of the PCE, for QW IBSCs and consequently intrinsic loss (IL) in QW IBSCs differ from those in QD IBSCs, calculated by Luque and Marti [15] and Arefinia [23], respectively, but they have not yet been studied. Driving FLE for QW IBSCs, in addition to developing physical insight and intuition, can open opportunities for future development and accelerate the fabrication of efficient QW IBSCs.

Extrinsic loss and IL limit the conversion efficiency in a SC. Extrinsic loss like contact shadowing, series resistances of different layers and electrical contacts, and shunt resistances of parasitic recombination resulting from defects in the active layer and manufacturing defects can be theoretically eliminated by improving SC quality [39], but IL, which stems from the laws of thermodynamics and quantum mechanics, is unavoidable even in an idealized SC [40,41] and determines the FLE. In this paper, we derive the FLE of QW IBSCs through the calculation of IL, consisting of five components, including below-band-gap ($L_{\text{below } E_g}$), thermalization (L_{th}), emission (L_{em}), Carnot (L_{Carnot}), and angle mismatch

*arefinia@tabrizu.ac.ir

(L_{mismatch}) components. The fraction of the incident solar radiation not lost via the IL components (ILCs) can be extracted as useful work, leading to the FLE. Therefore, the FLE of QW IBSCs is calculated by evaluating the ILCs, which are formulated using the principle of photon-electron detailed balance. The remainder of the paper is as follows. Before we explain the modeling of ILCs in QW IBSCs, a structure of QW IBSCs based on a published experimental report, which is an $\text{In}_x\text{Ga}_{1-x}\text{As}/\text{GaAs}$ QW IBSC, is introduced in Sect. II. Also, to understand how an IB is created in a QW IBSC, the energy-band diagram of the $\text{In}_x\text{Ga}_{1-x}\text{As}/\text{GaAs}$ QW IBSC is explained in Sec. III. Then, the ILCs in the QW IBSCs are modeled in Sec. IV. Finally, the relevant conclusions from the modeling of ILCs and consequently the FLE for the QW IBSCs are presented in Sect. V A, and the effect of indium content, diagonal length, and period of QWs on each ILC and consequently the FLE for $\text{In}_x\text{Ga}_{1-x}\text{As}/\text{GaAs}$ QW IBSCs, to be referred to as quantum engineering of ILCs and the FLE, are investigated in Sec. V B.

II. STRUCTURE OF THE $\text{In}_x\text{Ga}_{1-x}\text{As}/\text{GaAs}$ QW IBSC

A schematic view of a QW IBSC is shown in Fig. 1(a), where a standard undoped GaAs buffer is followed by an n -type ($N_D = 5.0 \times 10^{17} \text{ cm}^{-3}$) GaAs layer, on which there is a superlattice of undoped $\text{In}_x\text{Ga}_{1-x}\text{As}:\text{QWR}-\text{GaAs}:\text{barriers}$. Then, the structure is capped by p -type ($N_A = 5.0 \times 10^{17} \text{ cm}^{-3}$) GaAs. The $\text{In}_x\text{Ga}_{1-x}\text{As}$ QWs, with hexagonal cross section [42,43] in the x - y plane and height h_{QW} in the z direction, are parallel to each other. The distance between the axis of the hexagonal QWs in the x and y directions is L_1 and L_2 , respectively. Therefore, a unit cell of the $\text{In}_x\text{Ga}_{1-x}\text{As}:\text{QW}-\text{GaAs}:\text{barrier}$ structure, as shown in

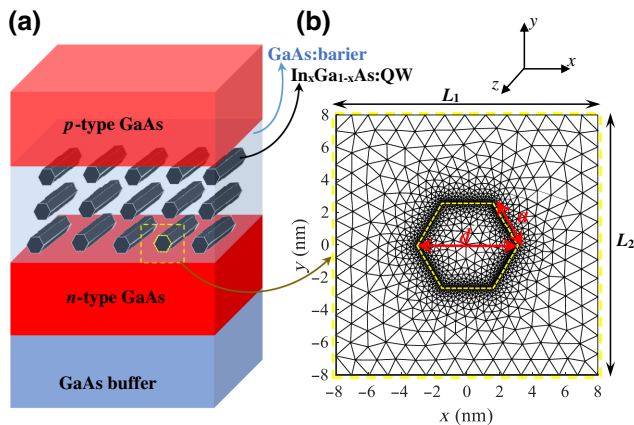


FIG. 1. (a) Structure of the $\text{In}_x\text{Ga}_{1-x}\text{As}/\text{GaAs}$ QW IBSC used in modeling. (b) A unit cell of the hexagonal- $\text{In}_x\text{Ga}_{1-x}\text{As}:\text{QW}-\text{GaAs}:\text{barrier}$ structure ($L_1=L_2=16 \text{ nm}$ and $d = 6 \text{ nm}$) with a constrained mesh in the x - y plane.

Fig. 1(b), is a rectangle (host material of GaAs) with sides of L_1 and L_2 in which there is a hexagon (the cross section of the unstrained hexagonal $\text{In}_x\text{Ga}_{1-x}\text{As}$ QW) with a diagonal length of d , a side length of $a = d/2$, and an area of $A = (1.5\sqrt{3})a^2$.

III. ENERGY-BAND DIAGRAM OF THE $\text{In}_x\text{Ga}_{1-x}\text{As}/\text{GaAs}$ QW IBSC

The energy-band diagram for the GaAs p - i - n junction with three $\text{In}_{0.7}\text{Ga}_{0.3}\text{As}$ QWs in the intrinsic region, for one of the two confined directions of the QWs, is depicted in Fig. 2 from knowledge of their electronic band structures. In the $\text{In}_x\text{Ga}_{1-x}\text{As}:\text{QW}-\text{GaAs}:\text{barrier}$ region, called the “IB region”, the electron potential wells (ΔE_C) are created by the energy difference between the conduction bands (CBs) of $\text{In}_x\text{Ga}_{1-x}\text{As}$ and GaAs. The hole potential wells (ΔE_V) are zero, because the offset of the valence bands (VBs), for the unstrained case of the $\text{In}_x\text{Ga}_{1-x}\text{As}/\text{GaAs}$ system [44] as obtained by Wei *et al.* [45], is zero.

The energy levels of an individual QW [i.e., the unit cell depicted in Fig. 1(b)] are calculated with use of the two-dimensional (2D) Schrödinger equation under the effective-mass approximation by means of the finite-element method (FEM) [24] in MATLAB, as briefly explained in Appendix A. To establish the numerical model, we calculate the energy levels of pyramid and truncated-pyramid QD structures introduced in Ref. [46] with the three-dimensional Schrödinger equation. The energy levels reported in Ref. [46] were reproduced by our calculations, showing the validity of the numerical model. We consider a traditional parabolic model for the CB in the effective-mass approximation. The effect of the CB nonparabolicity of $\text{In}_x\text{Ga}_{1-x}\text{As}$ on the energy levels was

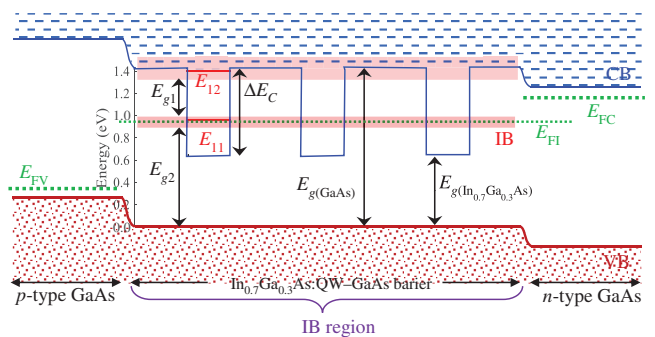


FIG. 2. p - i - n junction diagram and one-dimensional band profile (for the x direction or the y direction) of GaAs barriers with band gap $E_{g(\text{GaAs})}$ and three hexagonal $\text{In}_{0.7}\text{Ga}_{0.3}\text{As}$ QWs with $d=6 \text{ nm}$ and $L_1=L_2=16 \text{ nm}$ and with band gap $E_{g(\text{In}_{0.7}\text{Ga}_{0.3}\text{As})}$. ΔE_C is the CB offset, E_{11} and E_{12} are the energy levels of individual QWs, E_{g1} and E_{g2} are the sub-band gaps, and E_{FC} , E_{FV} , and E_{FI} are the quasi-Fermi-levels of the CB, VB, and IB, respectively.

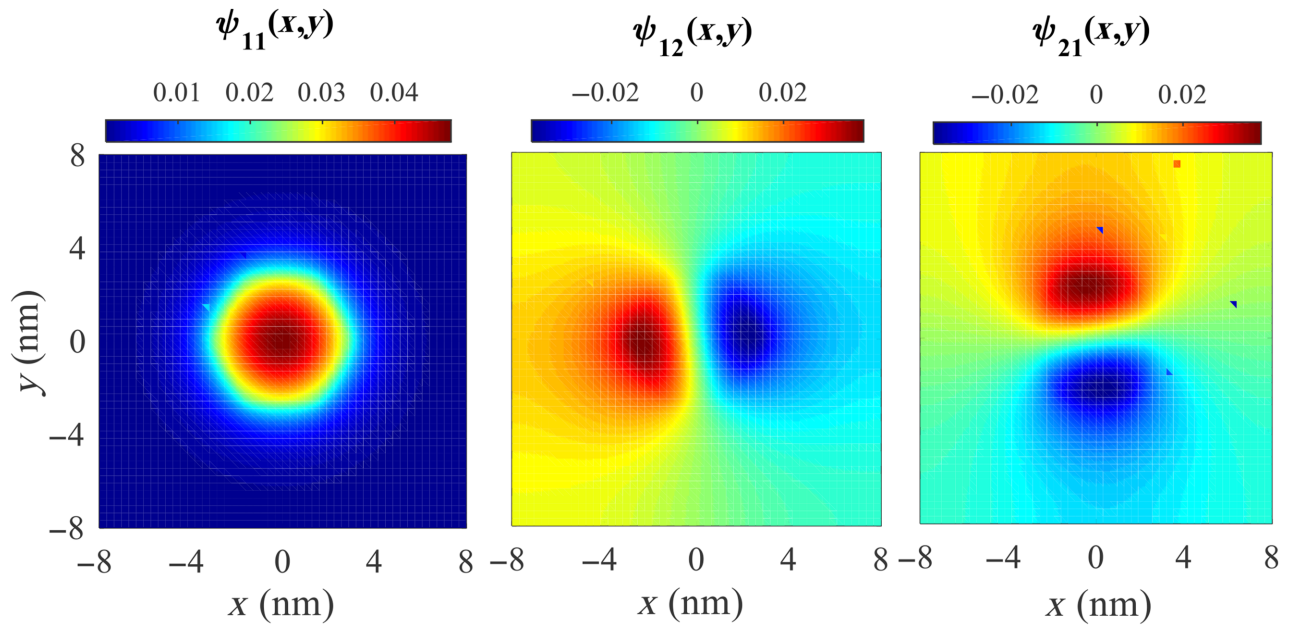


FIG. 3. CB wave functions of electrons for the first three energy levels ($E_{11}=0.32$ eV and $E_{12}=E_{21}=0.76$ eV) in hexagonal- $\text{In}_x\text{Ga}_{1-x}\text{As}$:QW-GaAs:barrier structure with $d=6$ nm and $L_1=L_2=16$ nm.

investigated by Tiutiunnyk *et al.* [47]. As an instance of the numerical model, the wave functions related to the energy levels of a unit cell with $d=6$ nm and $L_1=L_2=16$ nm, which are $E_{11}=0.32$ eV and $E_{12}=E_{21}=0.76$ eV, are displayed in Fig. 3.

For regularly spaced QWs, the coupling between QWs results in a splitting of quantized energy levels of individual QWs and the formation of 2D minibands. The width of 2D minibands is calculated with the Bloch approximation for a periodic potential function as explained by Slater *et al.* [48]. Calculation of miniband width related to Fig. 2 shows that the second miniband overlaps with the CB, and thus only the first miniband acts as an IB. The IB leads to the division of the band gap of the barrier material into two sub-band gaps, E_{g1} and E_{g2} . E_{g1} is the gap (energy difference) between the top edge of the IB and the bottom edge of the miniband arising from the second energy level. E_{g2} is the energy difference between the bottom edge of the IB and the top edge of the VB. The IB should be approximately half-filled to have both filled and empty states for promoting electrons to the CB and receiving electrons from the VB [49–51]. Therefore, the QW stack in the $\text{In}_x\text{Ga}_{1-x}\text{As}$ /GaAs QW IBSC must be δ doped with donor atoms to prefill the IB. Kunets *et al.* [27] considered Si n -type δ doping with a concentration that supplied one donor atom per QW.

Exposure of the QW IBSC to light leads to the splitting of the Fermi level into three quasi-Fermi-levels, E_{FC} , E_{FV} , and E_{FI} , related to the CB, VB, and IB, respectively [51–54], as shown in Fig. 2. With the assumptions of charge neutrality (the sum of electron densities of the CB and the

IB minus the hole density of the VB and the ionized-donor-atom density for prefilling the IB is zero) in the QW stack, equality of terminal voltage with the split between E_{FC} and E_{FV} , and extraction of current only via the CB and the VB and not via the IB, three quasi-Fermi-levels of E_{FC} , E_{FV} , and E_{FI} can be obtained numerically.

IV. MODELING OF THE ILCs IN QW IBSCs

The modeling of the ILCs in QW IBSCs is based on a photon-electron detailed-balance principle in which a single photon, if fully absorbed in any transition, promotes only one electron, all recombinations are radiative, and the IB leads to the creation of a single electron-hole pair through absorption of two sub-band-gap photons sequentially in which the first photon excites an electron from the VB to the IB and the second photon excites it from the IB to the CB. Therefore, the number of excited electrons is directly related to the number of incident photons. In this paper, multiple-exciton generation [55] and entropy losses associated with the dilution of excited electrons in the semiconductor band [56] are not considered.

For modeling of ILCs, the spectral photon flux, N , is considered by the generalized Planck blackbody law as

$$N(\varepsilon, T, \Theta, \mu) = \frac{2n^2\Theta}{c^2h^3} \frac{\varepsilon^2}{\exp[(\varepsilon - \mu)/kT] - 1}, \quad (1)$$

where ε is the energy, T is the temperature, Θ is the solid angle of emission (Θ_{emit}) or absorption (Θ_{abs}) [41], μ is the chemical potential, c is the light speed, n is the refractive

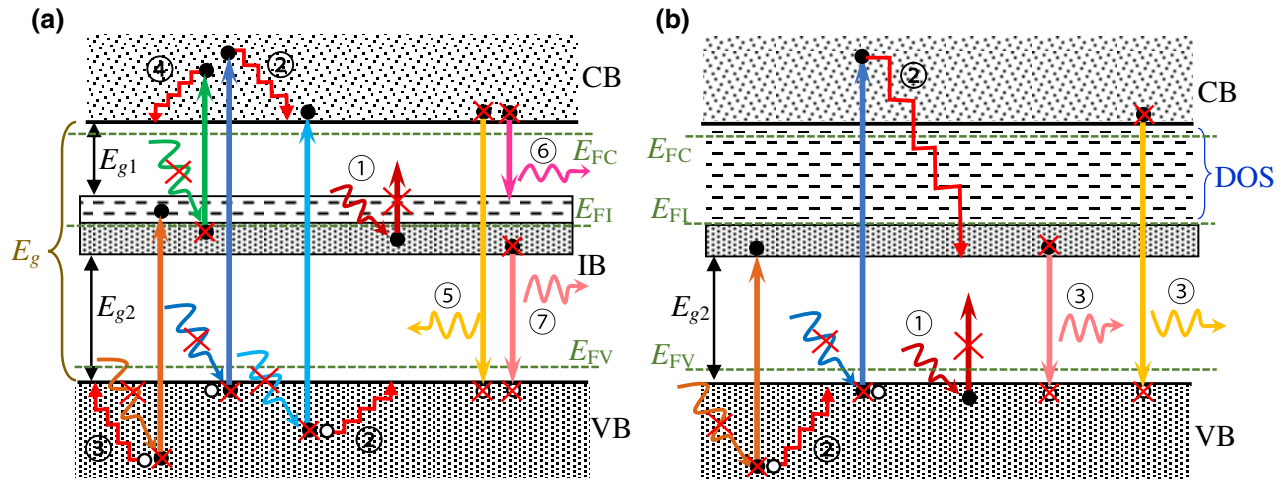


FIG. 4. (a) Energy-band diagram of the IB region for the confined transverse directions (x and y). Process 1 illustrates $L^x_{\text{below } E_g}$ or $L^y_{\text{below } E_g}$, process 2–4 illustrate L^x_{th} or L^y_{th} , and processes 5–7 illustrate L^x_{em} or (L^y_{em}) . (b) Energy-band diagram for the longitudinal z direction. Processes 1, 2, and 3 illustrate $L^z_{\text{below } E_g}$, L^z_{th} , and L^z_{em} , respectively.

index of the surroundings, h is Planck's constant, and k is Boltzmann's constant.

Considering that electrons in the QWs are confined in two transverse directions [x and y directions in Fig. 1(a)] and they are free in the longitudinal direction [z direction in Fig. 1(a)], the modeling of ILCs in QW IBSCs differs from that in QD IBSCs where the electrons are confined in three directions, as presented in Ref. [23]. However, the QW IBSCs as the QD IBSCs have to fulfill two essential criteria: (i) An extra photogenerated current resulting from the existence of IB has to be created by the utilization of sub-band-gap photons in a two-step absorption process. (ii) The output voltage has to be proportional to host semiconductor band gap (without the IB) and not to any of the two sub-band gaps. Not fulfilling these two criteria would imply that the solar cell cannot be as an IB-material candidate. In the experimental report on an $\text{In}_x\text{Ga}_{1-x}\text{As}/\text{GaAs}$ QW IBSC by Kunets *et al.* [27], both criteria were verified.

To model the ILCs in QW IBSCs, space decomposition is done as in Fig. 4 in which Fig. 4(a) shows the energy-band diagram of the IB region, the intrinsic region of the p - i - n SC incorporating QW stack, for two confined transverse directions (x and y), and Fig. 4(b) shows the energy-band diagram for the longitudinal z direction. In the x and y directions, the IB is formed [see Fig. 4(a)], but in the z direction, electrons can move freely, and therefore the energy states spread out into a continuous band with energies of $\hbar^2 k_z^2 / 2m^*$ (k_z is the wave vector in the z direction and m^* is the electron effective mass) [35]. Hence, as illustrated schematically in Fig. 4(b), we consider a continuous density of states (DOS) between the IB and the CB, but the specific shape of their wave functions is not taken into account.

According to photon absorption and emission depicted in Fig. 4 and considering $E_{g1} < E_{g2}$, the ILCs in the QW IBSCs are defined as follows:

(a) $L_{\text{below } E_g}$. $L_{\text{below } E_g}$ is the energy fraction of unabsorbed photons from the total photon-emission flux [23]. As shown in Fig. 4(a) by process 1, photons with energies less than E_{g1} cannot be absorbed, but photons with energies greater than E_{g1} are absorbed by one of the following transitions: $\text{IB} \rightarrow \text{CB}$, $\text{VB} \rightarrow \text{IB}$, or $\text{VB} \rightarrow \text{CB}$. Photons with the energies of $E_{g1} \leq \varepsilon < E_{g2}$, $E_{g2} \leq \varepsilon < E_g$, and $\varepsilon \geq E_g$ are, respectively, absorbed by the following transitions: $\text{IB} \rightarrow \text{CB}$, $\text{VB} \rightarrow \text{IB}$, and $\text{VB} \rightarrow \text{CB}$. Therefore, $L_{\text{below } E_g}$ in the x and y directions ($L^x_{\text{below } E_g}$ and $L^y_{\text{below } E_g}$) is determined by the number of photons with energies less than E_{g1} , as follows:

$$L^x_{\text{below } E_g} = L^y_{\text{below } E_g} = \frac{1}{P_{\text{in}}} \left(\frac{1}{3} \int_0^{E_{g1}} \varepsilon N(\varepsilon, T_{\text{Sun}}, \Theta_{\text{abs}}, \mu = 0) d\varepsilon \right), \quad (2)$$

where P_{in} is the input power related to the incident solar energy, T_{Sun} is the Sun temperature, and the coefficient $1/3$ represents the portion of each direction.

For the z direction, as depicted in Fig. 4(b) by process 1, photons with energies less than E_{g2} cannot be absorbed and photons with energies $\varepsilon \geq E_{g2}$ are absorbed due to the DOS lying between the IB and the CB. Therefore, $L^z_{\text{below } E_g}$ is determined by the number of photons with energies less than E_{g2} as

$$L^z_{\text{below } E_g} = \frac{1}{P_{\text{in}}} \left(\frac{1}{3} \int_0^{E_{g2}} \varepsilon N(\varepsilon, T_{\text{Sun}}, \Theta_{\text{abs}}, \mu = 0) d\varepsilon \right). \quad (3)$$

Therefore, $L_{\text{below } E_g}$ in QW IBSCs is given by

$$\begin{aligned} L_{\text{below } E_g} &= L_{\text{below } E_g}^x + L_{\text{below } E_g}^y + L_{\text{below } E_g}^z \\ &= \frac{1}{P_{\text{in}}} \left(\frac{2}{3} \int_0^{E_{g1}} \varepsilon N(\varepsilon, T_{\text{Sun}}, \Theta_{\text{abs}}, \mu = 0) d\varepsilon \right. \\ &\quad \left. + \frac{1}{3} \int_0^{E_{g2}} \varepsilon N(\varepsilon, T_{\text{Sun}}, \Theta_{\text{abs}}, \mu = 0) d\varepsilon \right). \end{aligned} \quad (4)$$

(b) L_{th} . Processes 2–4 in Fig. 4(a) describe L_{th} for the x and y directions. Process 2 explains that absorbed photons with energies greater than the host-material band gap (E_g) that excite an electron from the VB to the CB have the same effect as an absorbed photon with energy E_g , and the extra energy exceeding the energy transition of E_g is lost by a thermal phonon [23]. Also, as shown by process 3 (process 4), electron-hole pairs created by the absorbed photons with energies $E_{g2} \leq \varepsilon < E_g$ ($E_{g1} \leq \varepsilon < E_{g2}$) lose their excessive energies [i.e., difference between photon energy and the sub-band gap E_{g2} (E_{g1})] in the form of phonons. Therefore, L_{th}^x and L_{th}^y consist of three terms as follows:

$$\begin{aligned} L_{\text{th}}^x &= L_{\text{th}}^y = \frac{1}{P_{\text{in}}} \\ &\quad \times \frac{1}{3} \left(\int_{E_{g1}}^{E_{g2}} (\varepsilon - E_{g1}) N(\varepsilon, T_{\text{Sun}}, \Theta_{\text{abs}}, \mu = 0) d\varepsilon \right. \end{aligned}$$

$$\begin{aligned} L_{\text{th}} &= L_{\text{th}}^x + L_{\text{th}}^y + L_{\text{th}}^z = \frac{1}{P_{\text{in}}} \left[\frac{2}{3} \left(\int_{E_{g1}}^{E_{g2}} (\varepsilon - E_{g1}) N(\varepsilon, T_{\text{Sun}}, \Theta_{\text{abs}}, \mu = 0) d\varepsilon + \int_{E_{g2}}^{E_g} (\varepsilon - E_{g2}) N(\varepsilon, T_{\text{Sun}}, \Theta_{\text{abs}}, \mu = 0) d\varepsilon \right. \right. \\ &\quad \left. \left. + \int_{E_g}^{\infty} (\varepsilon - E_g) N(\varepsilon, T_{\text{Sun}}, \Theta_{\text{abs}}, \mu = 0) d\varepsilon \right) + \frac{1}{3} \left(\int_{E_{g2}}^{\infty} (\varepsilon - E_{g2}) N(\varepsilon, T_{\text{Sun}}, \Theta_{\text{abs}}, \mu = 0) d\varepsilon \right) \right]. \end{aligned} \quad (7)$$

(c) L_{em} . As shown in Fig. 4(a) by process 5 for the transverse directions, the generated electrons in the CB that reach the edge of the CB can relax back down to the VB and recombine with the holes through photon emission. Furthermore, the electrons in the edge of the CB can come down to the IB (process 6) and the IB electrons can come down to the VB (process 7) by emitting photons. For the longitudinal direction, process 3 in Fig. 4(b) shows that the electrons that reach the edge of sub-band

$$\begin{aligned} L_{\text{em}} &= \frac{1}{P_{\text{in}}} \left[\frac{2}{3} \left(E_{g1} \int_{E_{g1}}^{E_{g2}} N(\varepsilon, T_{\text{cell}}, \Theta_{\text{emit}}, \mu = (E_{\text{FC}} - E_{\text{FI}})_M) d\varepsilon + E_{g2} \int_{E_{g2}}^{E_g} N(\varepsilon, T_{\text{cell}}, \Theta_{\text{emit}}, \mu = (E_{\text{FI}} - E_{\text{FV}})_M) d\varepsilon \right. \right. \\ &\quad \left. \left. + E_g \int_{E_g}^{\infty} N(\varepsilon, T_{\text{cell}}, \Theta_{\text{emit}}, \mu = (E_{\text{FC}} - E_{\text{FV}})_M) d\varepsilon \right) + \frac{1}{3} \left(E_{g2} \int_{E_{g2}}^{\infty} N(\varepsilon, T_{\text{cell}}, \Theta_{\text{emit}}, \mu = (E_{\text{FI}} - E_{\text{FV}})_M) d\varepsilon \right) \right], \end{aligned} \quad (8)$$

$$\begin{aligned} &+ \int_{E_{g2}}^{E_g} (\varepsilon - E_{g2}) N(\varepsilon, T_{\text{Sun}}, \Theta_{\text{abs}}, \mu = 0) d\varepsilon \\ &+ \int_{E_g}^{\infty} (\varepsilon - E_g) N(\varepsilon, T_{\text{Sun}}, \Theta_{\text{abs}}, \mu = 0) d\varepsilon \Big), \end{aligned} \quad (5)$$

where the first, second, and third integrals on the right-hand side are, respectively, related to thermalization loss described by processes 4, 3, and 2 in Fig 4(a), and the coefficient 1/3 represents the portion of each direction.

For the z direction, as shown in Fig. 4(b) by process 2, energy difference between absorbed photon ($\varepsilon > E_{g2}$) and the sub-band gap E_{g2} is lost in the thermalization process, where the generated hole thermalizes from the VB to its edge and the generated electron relaxes to the IB edge due to the DOS lying between the CB and the IB. Therefore, L_{th}^z has only one term as follows:

$$L_{\text{th}}^z = \frac{1}{P_{\text{in}}} \times \frac{1}{3} \left(\int_{E_{g2}}^{\infty} (\varepsilon - E_{g2}) N(\varepsilon, T_{\text{Sun}}, \Theta_{\text{abs}}, \mu = 0) d\varepsilon \right). \quad (6)$$

Thus, L_{th} in QW IBSCs is computed as

gap E_{g2} through the available DOS between the CB and the IB can recombine with the VB holes. The energy lost through photon emission, L_{em} , in each process, process 5, 6, or 7 in Fig. 4(b) and process 3 in Fig. 4(b), is defined by the number of emitted photons in that process multiplied by the band (sub-band) gap for the transitions in that process [23]. Therefore, emission loss, L_{em} , in QW IBSCs can be calculated as

where the first, second, and third terms in first large parentheses on the right-hand side are, respectively, related to the portion of L_{em} depicted by processes 6, 7, and 5 in Fig. 4(a) and the term in the second large parentheses on the right-hand side is related to the portion of L_{em} depicted by process 3 in Fig. 4(b). The coefficients $2/3$ and $1/3$, as explained for $L_{below\ E_g}$ and L_{th} , are the portion of the transverse and longitudinal directions, respectively. The subscript M in the definition of μ for each term indicates that the three quasi-Fermi-levels of E_{FC} , E_{FV} , and E_{FI} are related to the applied voltage, which is $V = (E_{FC} - E_{FV})/q$, at the maximum power point. V_M is obtained by application of the detailed-balance principle to determine the maximum PCE for QW IBSCs, as explained in Appendix B.

(d) $L_{mismatch}$. The energy loss associated with the entropy generation resulting from the mismatch between the solid angles of absorption and emission is expressed by the angle mismatch loss, $L_{mismatch}$, as follows [57–59]:

$$L_{mismatch} = \frac{1}{P_{in}} \frac{kT_{cell}}{q} \ln \left(\frac{\Theta_{emit}}{\Theta_{abs}} \right) J_M, \quad (9)$$

where q is the electron charge, T_{cell} is the QW-IBSC temperature, and J_M is the current density at the maximum power point, described in Appendix B.

(e) L_{Carnot} . The QW IBSC at temperature T_{cell} absorbs energy through absorbed photons, and its entropy increases. At the same time, the Sun at temperature T_{Sun} loses energy due to emitted photons, and its entropy decreases. The increase in entropy of the QW IBSC is greater than the decrease in entropy of the Sun, because $T_{cell} < T_{Sun}$. The energy needed to evacuate the entropy of the system is expressed by Carnot loss [23,60] as follows:

$$L_{Carnot} = \frac{1}{P_{in}} \frac{E_g}{q} \frac{T_{cell}}{T_{Sun}} J_M. \quad (10)$$

L_{Carnot} is influenced by the fundamental band gap E_g and not by any of the two sub-band gaps, neither E_{g1} nor E_{g2} .

Finally, the FLE (η_F) is defined by the fraction of solar energy not lost via IL as

$$\eta_F = 1 - (L_{below\ E_g} + L_{th} + L_{em} + L_{mismatch} + L_{Carnot}). \quad (11)$$

V. RESULTS AND DISCUSSION

The results are presented in two subsections. In the first subsection, the ILCs and FLE are computed for nonspecific QW IBSCs. Because there are no material parameters for the nonspecific cases, the bandwidth of the IB is ignored in the first subsection and therefore the sum of E_{g1} and E_{g2} is equal to the fundamental band gap E_g . In the second subsection, they are calculated for $In_xGa_{1-x}As/GaAs$

QW IBSCs. The bandwidth of the IB is calculated with the Bloch method of a periodic potential function described by Slater *et al.* [48].

A. ILCs and FLE for nonspecific QW IBSCs

The sub-band-gap dependence of ILCs in QW IBSCs is depicted in Figs. 5(a)–5(e). As can be seen from Fig. 5(a), with increasing fundamental band gap E_g through increasing sub-band gap E_{g2} and keeping sub-band gap E_{g1} constant, $L_{below\ E_g}$, arising from the transmission loss of unabsorbed photons, increases due to an increase in $L^z_{below\ E_g}$, and with increasing E_g through increasing E_{g1} and keeping E_{g2} constant, $L_{below\ E_g}$ increases due to the increase in $L^x_{below\ E_g}$ and $L^y_{below\ E_g}$. For constant E_g , the shifting of the IB position leads to the changing of E_{g1} and consequently $E_{g2} = E_g - E_{g1}$, and as a result, as seen in Fig. 6(a), $L_{below\ E_g}$ is minimized in an E_{g1} .

Figure 5(b) shows L_{th} as a function of E_{g1} and E_{g2} . A considerable decrease in L_{th} is seen with increasing fundamental band gap E_g through increasing both sub-band gaps E_{g1} and E_{g2} . Also, increasing E_g through increasing E_{g1} and keeping E_{g2} constant or through increasing E_{g2} and keeping E_{g1} constant decreases L_{th} . While the former decrease is due the decrease in L^x_{th} and L^y_{th} , the latter is due the decrease in L^z_{th} . But, for constant E_g , the variation of E_{g1} and E_{g2} with IB-position shifting leads to a minimized L_{th} for optimum E_{g1} and E_{g2} , as seen in Fig. 6(b).

The dependency of L_{Carnot} and $L_{mismatch}$ on E_{g1} and E_{g2} is depicted in Figs. 5(c) and 5(d), respectively. It is found that increasing E_g through increasing both E_{g1} and E_{g2} or increasing one sub-band gap and keeping the other sub-band gap constant reduces $L_{mismatch}$ and increases L_{Carnot} . An increase in both sub-band gaps or one of the sub-band gaps leads to a decrease in the energy range for photon absorption and consequently a decrease in number of the photogenerated carriers and ultimately J_M reduction. Because of the direct relationship between $L_{mismatch}$ and J_M , reduction of J_M leads to reduction of $L_{mismatch}$, but L_{Carnot} depends on E_g , in addition to J_M . Therefore, the combined effects of J_M reduction and E_g increase lead to L_{Carnot} increase. For constant E_g , increasing E_{g1} leads to J_M reduction and consequently reduction of both $L_{mismatch}$ and L_{Carnot} , as seen in Figs. 6(c) and 6(d), respectively.

It is found from Fig. 5(e) that among the ILCs, the least portion of IL is related to L_{em} , and for most configurations of two sub-band gaps of QW IBSCs it is less than 1%.

Calculation results for the FLE of QW IBSCs, displayed in Fig. 5(f), show that the maximum FLE is approximately 42%, occurring at various configurations of sub-band gaps in the range from 0.77 to 0.87 eV for E_{g1} and from 1.3 to 1.43 eV for E_{g2} . In these sub-band gaps, the sum of ILCs, which is equal to $IL = 100\% - 42\% = 58\%$, is minimized.

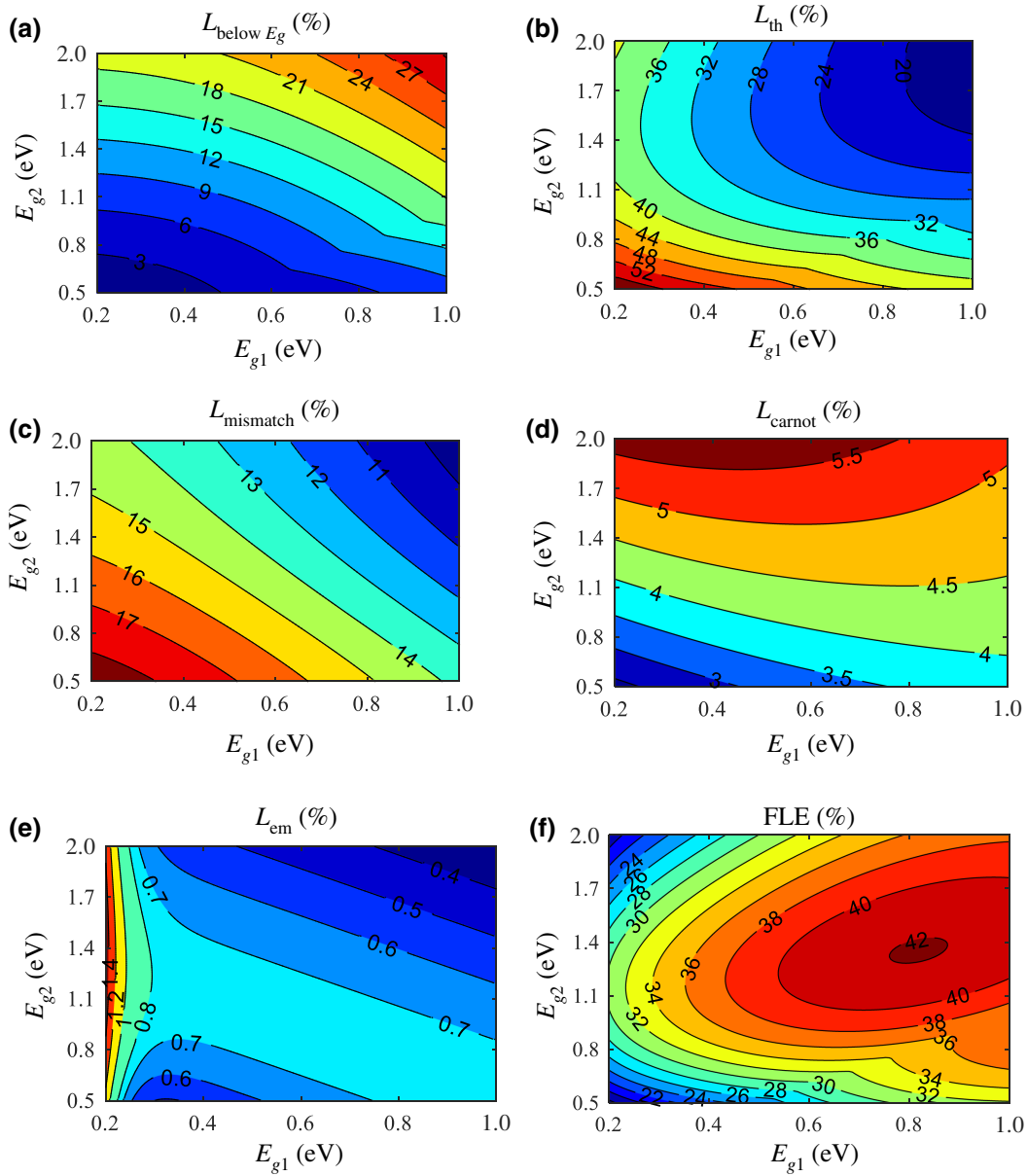


FIG. 5. (a) $L_{\text{below } E_g}$, (b) L_{th} , (c) L_{mismatch} , (d) L_{carnot} , (e) L_{em} , and (f) FLE for the QW IBSCs versus sub-band gaps E_{g1} and E_{g2} .

In comparison with QD IBSCs with a maximized FLE of 47% (minimized IL of 53%) in the sub-band intervals of 0.6–1.07 eV for E_{g1} and 1.03–1.75 eV for E_{g2} [23] and with the conventional single-band-gap SCs with a maximized FLE of 32.5% (minimized IL of 67.5%) in an optimized band gap of 1.31 eV [57], the FLE for QW IBSCs is greater than for conventional single-band-gap SCs but less than for QD IBSCs. In addition, the sub-band-configuration intervals of QW IBSCs with maximized FLE are narrower than those of QD IBSCs. Although the maximized FLE for QW IBSCs is less than that for QD IBSCs, they can achieve better performance due to some advantages of QWs over QDs, as mentioned in Sec. I.

It is to be noted that the experimental values of the PCE for fabricated QW IBSCs or QD IBSCs are far less than their optimized FLE [20,61,62].

B. Quantum engineering of ILCs and FLE for $\text{In}_x\text{Ga}_{1-x}\text{As}/\text{GaAs}$ QW IBSCs

In this subsection, the percentage of each ILC and the FLE for $\text{In}_x\text{Ga}_{1-x}\text{As}/\text{GaAs}$ QW IBSC are calculated. For $\text{In}_x\text{Ga}_{1-x}\text{As}$ QWs, $d=6$ nm and $L_1=L_2=16$ nm are considered in the calculations, unless otherwise stated. Furthermore, the dependence of ILCs and the FLE on the indium mole fraction, diagonal length, and period of QWs is investigated. The aforementioned parameters offer a way

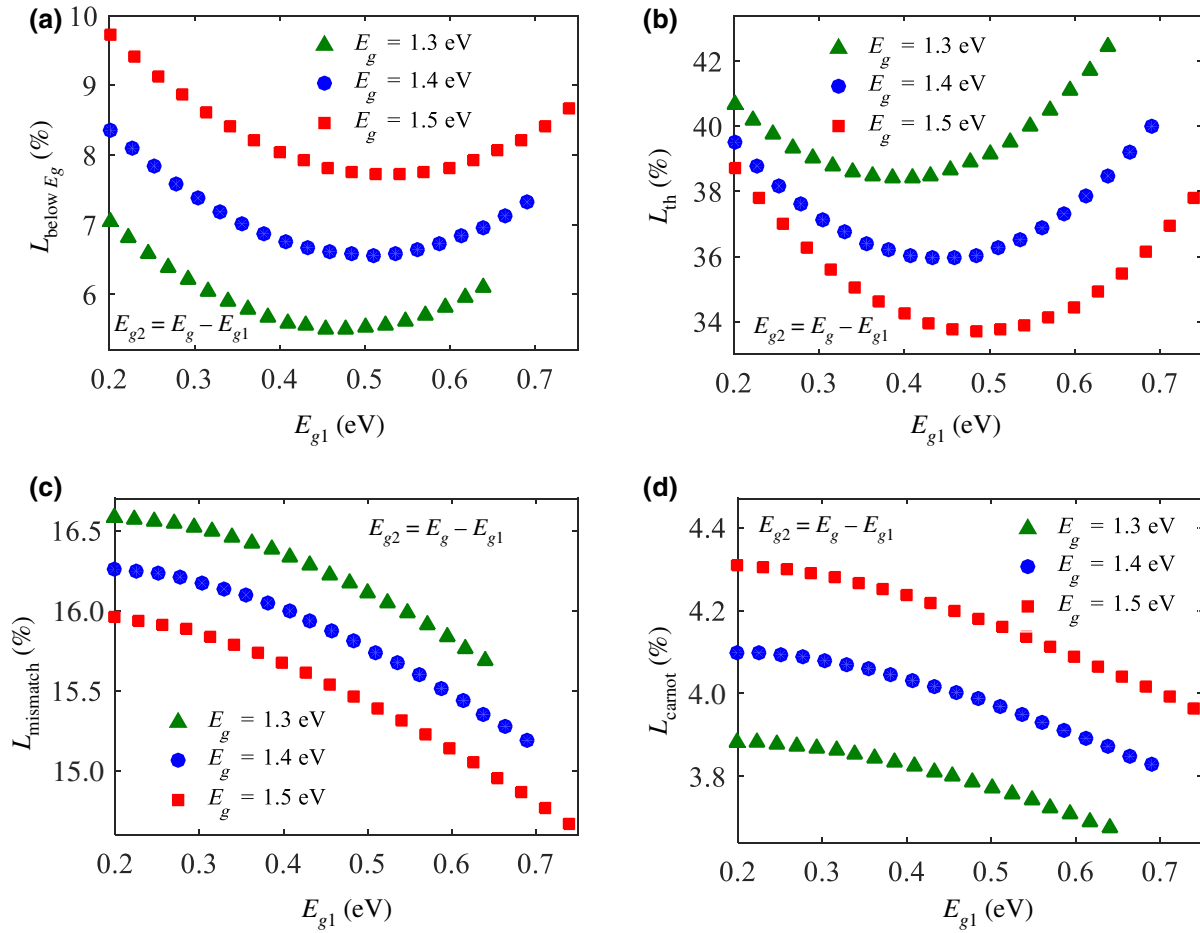


FIG. 6. (a) $L_{\text{below } E_g}$, (b) L_{th} , (c) L_{mismatch} , and (d) L_{cannot} for constant fundamental band gaps $E_g = 1.3, 1.4,$ and 1.5 eV as a function of sub-band gap E_{g1} . At each E_{g1} value, E_{g2} is $E_g - E_{g1}$.

for engineering the energy states confined in QWs and consequently the placement and width of the IB and ultimately the ILCs and the FLE of $\text{In}_x\text{Ga}_{1-x}\text{As}/\text{GaAs}$ QW IBSCs, so we have referred to this subsection as “quantum engineering of ILCs and the FLE”.

The effect of indium content, x , on the ILCs and FLE of $\text{In}_x\text{Ga}_{1-x}\text{As}/\text{GaAs}$ QW IBSCs is depicted in Fig. 7 for $x \geq 0.3$. Calculation results show that for $x < 0.3$, the IB overlaps with the CB, and the sub-band gap E_{g1} between the CB and the IB did not open. It is seen from Fig. 7 that L_{th} is the most dominant fraction of IL in the QW IBSCs, and L_{mismatch} is the second ILC with a considerable portion.

The sub-band configurations of E_{g1} and E_{g2} for $\text{In}_x\text{Ga}_{1-x}\text{As}/\text{GaAs}$ QW IBSCs can be engineered by changing x , as depicted in Fig. 8 for the fundamental band gap of E_g (GaAs). It is found that with increasing x , E_{g1} increases and E_{g2} decreases. QWs with higher indium content create larger ΔE_C , as shown in Fig. 8, and therefore the first energy level, which determines the position of the IB, comes down, and as a result E_{g1} becomes wider and E_{g2} becomes narrower. Hence, the sub-band configuration

leads to a maximum FLE of approximately 35% or a minimum IL of approximately 65% for indium content of $0.5 < x \leq 1$, as seen in Fig. 7. Therefore, in the remainder of this paper, we choose $x = 0.7$.

In a constant unit cell with $L_1 = L_2 = 16$ nm, the effect of QW size on the ILCs and FLE of $\text{In}_{0.7}\text{Ga}_{0.3}\text{As}/\text{GaAs}$ QW IBSCs is investigated, where the diagonal length (d) of hexagonal QWs is varied. We consider $d \geq 3$ nm in Fig. 9, because for $d < 3$ nm the first miniband in the QWs overlaps with the CB, and therefore the IB does not appear. Different sub-band configurations of E_{g1} and E_{g2} for different d values lead to the maximum FLE or the minimum IL at $d = 6$ nm. Increasing d from 3 to 6 nm leads to a wider E_{g1} and a narrower E_{g2} , but for $d > 6$ nm, the trend is reversed. For $d \leq 6$ nm, increasing d , which is equivalent to a decrease in quantum confinement, leads to the downshifting of the IB position and increase of the IB width. Therefore, the energy difference between the bottom of the CB and the top of the IB, E_{g1} , becomes larger, and the energy difference between the bottom of the IB and the top of the VB, E_{g2} , becomes smaller. For $d > 6$ nm, two

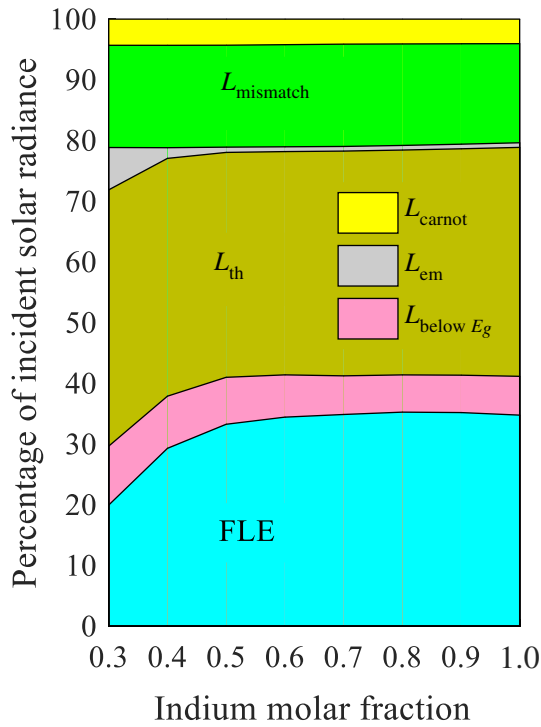


FIG. 7. The percentage of the incident solar radiation that each ILC process in the $\text{In}_x\text{Ga}_{1-x}\text{As}/\text{GaAs}$ QW IBSC consumes and hence, FLE under one-sun illumination in the $\text{In}_x\text{Ga}_{1-x}\text{As}/\text{GaAs}$ QW IBSCs are shown to be dependent on as a function of indium molar fraction, x .

minibands appears in the QWs, where the second miniband overlaps with the CB, and with increasing d , the minibands with an increase in width come down, and as a result, E_{g1} defined as the energy difference between the top of the first miniband, the IB, and the bottom of the second miniband, becomes narrower. Therefore, maximum E_{g1} at $d=6$ nm results in the minimum L_{th} and $L_{mismatch}$ and consequently the minimum IL or the maximum FLE, as seen in Fig. 9.

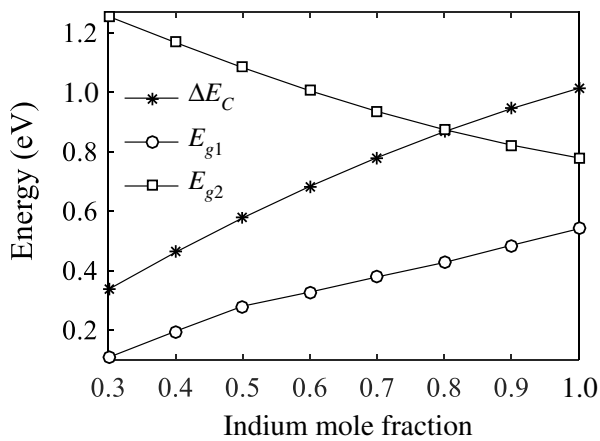


FIG. 8. ΔE_C , E_{g1} , and E_{g2} versus indium mole fraction, x , for $\text{In}_x\text{Ga}_{1-x}\text{As}/\text{GaAs}$ QW IBSCs.

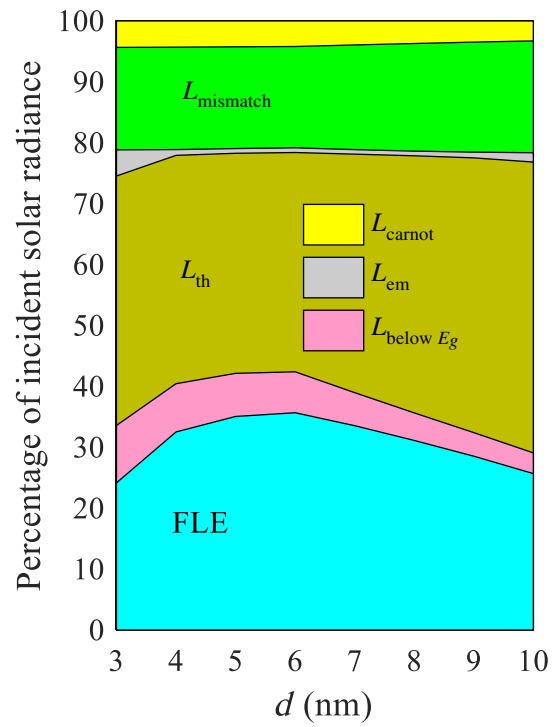


FIG. 9. The percentage of incident solar radiation that each ILC process in the $\text{In}_{0.7}\text{Ga}_{0.3}\text{As}/\text{GaAs}$ QW IBSC consumes and hence, FLE under one-sun illumination in the $\text{In}_{0.7}\text{Ga}_{0.3}\text{As}/\text{GaAs}$ QWIBSCs are shown to be dependent on as a function of the QWs diagonal length of QWs, d .

By fixing the diagonal length of QWs at $d=6$ nm, we show the effect of the distance between QWs, $L_1=L_2=L$, on the ILCs and FLE in Fig. 10. Changing L influences mainly the width of the IB such that wider IB is related to smaller L due to stronger electronic coupling. A high decrease in L can increase the IB width so that it overlaps with the CB leading to not creating the E_{g1} ; therefore, there has to be a minimum L to prevent the overlapping of the IB and CB. On the other hand, as L increases, the IB width decreases such that no IB is formed for very large L . Therefore, the maximum L at which there is electronic coupling between the localized states of QWs for forming the IB with acceptable width has to be determined. To meet these conditions, L is increased from 8 to 24 nm. With increasing L , the IB position goes up but the IB width decreases, leading to a slight increase in E_{g1} and E_{g2} . Therefore, there is a slight increase in $L_{below E_g}$ and L_{Carnot} and a slight decrease in $L_{mismatch}$ and L_{th} , leading to a slight increase in the FLE with increasing L . It can be seen from Fig. 10 that the $\text{In}_{0.7}\text{Ga}_{0.3}\text{As}/\text{GaAs}$ QW IBSC with QWs with $d=6$ and $L_1=L_2=24$ nm has minimum IL of 63.42% ($L_{below E_g}=7.23\%$, $L_{th}=34.78\%$, $L_{mismatch}=16.36\%$, $L_{Carnot}=4.28\%$, and $L_{em}=0.77\%$) and consequently maximum FLE of 36.58%. Comparing this value with the optimal FLE for QW IBSCs (approximately

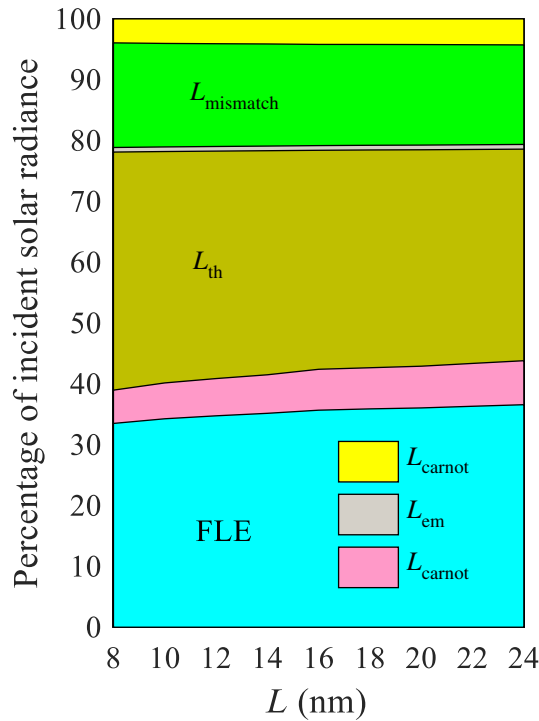


FIG. 10. The percentage of incident solar radiation that each ILC process in the $\text{In}_{0.7}\text{Ga}_{0.3}\text{As}/\text{GaAs}$ QW IBSC consumes and hence, FLE under one-sun illumination in the $\text{In}_{0.7}\text{Ga}_{0.3}\text{As}/\text{GaAs}$ QWIBSCs are shown to be dependent on as a function of the period length of QWs, L .

42%), one can be concluded that the material system of the experimentally reported QW IBSC ($\text{In}_x\text{Ga}_{1-x}\text{As}/\text{GaAs}$) is not the best choice. Therefore, searching for material systems of QWs and barriers with optimal material parameters required for efficient QW IBSCs, as done for QD IBSCs [24,63], remains a true challenge. The theoretical calculations in this paper can be applied to find candidate materials for implementing wide-band-gap QW IBSCs with an improved sub-band-gap distribution compared with the $\text{In}_x\text{Ga}_{1-x}\text{As}/\text{GaAs}$ case.

VI. CONCLUSIONS

An analytical formula for each ILC in QW IBSCs is obtained by the detailed-balance approach in connection with the mechanism of absorption and emission of photons in two confined directions and one free direction of carriers in the QWs. As a consequence of ILC calculation, an optimized FLE of approximately 42% is obtained for the QW IBSCs. Then, the ILCs and FLE for an experimentally reported QW-IBSC structure, which is a GaAs p - i - n junction with an array of $\text{In}_x\text{Ga}_{1-x}\text{As}$ QWs in the intrinsic layer, are calculated. To achieve this, by means of MATLAB, the 2D Schrödinger equation is solved by a FEM technique to obtain the IB position in the band gap of GaAs, and

the Bloch approximation of the periodic potential function is used to obtain the IB width. The results show that with optimized parameters of QW size and period length, a maximum FLE of approximately 37% and subsequently a minimum IL of approximately 63% are obtained for the $\text{In}_{0.7}\text{Ga}_{0.3}\text{As}/\text{GaAs}$ QW IBSC under 1-sun illumination.

APPENDIX A. APPLYING THE FEM TO THE 2D SCHRÖDINGER EQUATION

The first step in applying the FEM is the discretization of the physical region. Therefore, on the basis of the Delaunay triangulation algorithm, the unit cell of the $\text{In}_x\text{Ga}_{1-x}\text{As}:\text{QW}-\text{GaAs}:\text{barrier}$ structure is discretized into triangular elements and nodes with iterative improvement of the location of the nodes [64]. In the region near the interface of the two materials, where the results have to be more accurate than in other areas, smaller elements are produced, as seen in Fig. 1(b), to increase the number of evaluations.

The second step is reformulating the Schrödinger equation into a variational problem to use mesh elements, and then the variational problem is converted to a matrix problem by use of the geometry defined in the first step. With considering of a variation of the wave function, $\Psi(x,y)$, the Schrödinger equation, derived from the action integral, is expressed as

$$\delta \iint_{\Omega} \left(\frac{\hbar^2}{2m_e^*(x,y)} (\nabla \Psi(x,y))^* (\nabla \Psi(x,y)) + \Psi^*(x,y) V(x,y) \Psi(x,y) - \Psi^*(x,y) E \Psi(x,y) \right) d\Omega = 0, \quad (\text{A1})$$

where $\Psi(x,y)$ is the electron wave function, E is the energy, and $m_e^*(x,y)$ and $V(x,y)$ are the effective mass and potential energy of an electron, respectively, defined for a unit cell as

$$m_e^*(x,y) = \begin{cases} m_{\text{In}_x\text{Ga}_{1-x}\text{As}}^* & \text{inside the QW,} \\ m_{\text{GaAs}}^* & \text{outside the QW,} \end{cases} \quad (\text{A2})$$

$$V(x,y) = \begin{cases} \Delta E_C = E_{g(\text{GaAs})} - E_{g(\text{In}_x\text{Ga}_{1-x}\text{As})} & \text{inside the QW,} \\ 0 & \text{outside the QW,} \end{cases} \quad (\text{A3})$$

where $m_{(\text{GaAs})}^+$ and $E_g(\text{GaAs})$ are the electron effective mass and band gap of the barrier material, respectively, and $m_{\text{In}_x\text{Ga}_{1-x}\text{As}}^* = (0.067 - 0.056x + 0.01x^2)m_e$ [65] and $E_{g(\text{In}_x\text{Ga}_{1-x}\text{As})} = 0.4105 + 0.6337x + 0.475x^2$ [66] are the electron effective mass and band gap of the QW material, respectively.

$\Psi(x,y)$ is a summation of elemental wave functions, $\Psi_n(x,y)$, over all triangular elements. To calculate $\Psi_n(x,y)$,

the idea of transformation to a canonical element, where each triangular element having coordinates (x_i, y_i) , $i=1,2,3$, in the physical x - y plane is linearly mapped to a canonical element in a computational μ - ν plane, is applied. The canonical element is a three-node triangle having coordinates $(0,0)$, $(1,0)$, and $(0,1)$ in the μ - ν plane.

The transformation of coordinates and the transformation of $\Psi_n(x,y)$ from the physical x - y plane to the computational μ - ν plane are expressed by a linear combination of a finite set of basis functions, $\varphi_i^n(\mu, \nu)$, as

$$x = \sum_{i=1}^3 x_i \varphi_i^n(\mu, \nu), \quad y = \sum_{i=1}^3 y_i \varphi_i^n(\mu, \nu), \quad (\text{A4})$$

$$\Psi_n(x,y) = \sum_{i=1}^3 \psi_i^n \varphi_i^n(\mu, \nu), \quad (\text{A5})$$

where ψ_i^n is the unknown wave function amplitude at node i . It is worth mentioning that there are three basis functions comprising piecewise polynomial functions, $\varphi_i^n(\mu, \nu) = a_i^n \mu + b_i^n \nu + c_i^n$, with nine constants, a_i^n , b_i^n , and c_i^n , to be determined. Then, by transformation of the potential energy, $V(x,y)$, to the computational μ - ν plane, $V(\mu, \nu)$, the Schrödinger equation in a matrix representation will be constructed from

$$\begin{aligned} & \sum_{n=1}^{N_\Omega} \sum_{i=1}^3 \psi_i^{n*} \left(\frac{\hbar^2}{2m_e^*} \iint_{\Omega_n} (\nabla \varphi_i^n(\mu, \nu))^* (\nabla \varphi_j^n(\mu, \nu)) d\Omega \right) \psi_j^n + \sum_{n=1}^{N_\Omega} \sum_{i=1}^3 \psi_i^{n*} \left(\iint_{\Omega_n} \varphi_i^{n*}(\mu, \nu) V(\mu, \nu) \varphi_j^n(\mu, \nu) d\Omega \right) \psi_j^n \\ & = E \sum_{n=1}^{N_\Omega} \sum_{i=1}^3 \psi_i^{n*} \left(\iint_{\Omega_\alpha} \varphi_i^{n*}(\mu, \nu) \varphi_j^n(\mu, \nu) d\Omega \right) \psi_j^n, \end{aligned} \quad (\text{A6})$$

where N_Ω is the number of elements, Ω_α is the area of an element, and E is related to the energy levels of electrons. After transformation of the above differential equation into a matrix representation, it is solved to obtain the energy states and corresponding wave functions.

APPENDIX B. CALCULATING V_M AND J_M

The detailed-balance PCE of a QW IBSC is calculated by the power density delivered by the QW IBSC to an

external circuit (P_{out}), defined as the current density (J) multiplied by the applied voltage across the QW IBSC (V), divided by the power density received by the QW IBSC from the Sun (P_{in}).

J is equal to the charge-carrier flux, the number of electron-hole pairs collected at the contacts (N_{e-h}) multiplied by the electric charge q , and N_{e-h} is equal to the net photon flux, which is the difference between absorbed and emitted photons. Therefore, J is computed as

$$\begin{aligned} J = \frac{2}{3} & \left[\left(\int_{E_{g1}}^{E_{g2}} N(\varepsilon, T_{\text{Sun}}, \Theta_{\text{abs}}, \mu = 0) d\varepsilon - \int_{E_{g1}}^{E_{g2}} N(\varepsilon, T_{\text{cell}}, \Theta_{\text{emit}}, \mu_1) d\varepsilon \right) \right. \\ & + \left(\int_{E_{g2}}^{E_g} N(\varepsilon, T_{\text{Sun}}, \Theta_{\text{abs}}, \mu = 0) d\varepsilon - \int_{E_{g2}}^{E_g} N(\varepsilon, T_{\text{cell}}, \Theta_{\text{emit}}, \mu_2) d\varepsilon \right) \\ & + \left. \left(\int_{E_g}^{\infty} N(\varepsilon, T_{\text{Sun}}, \Theta_{\text{abs}}, \mu = 0) d\varepsilon - \int_{E_g}^{\infty} N(\varepsilon, T_{\text{cell}}, \Theta_{\text{emit}}, \mu_T) d\varepsilon \right) \right] \\ & + \frac{1}{3} \left(\int_{E_{g2}}^{\infty} N(\varepsilon, T_{\text{Sun}}, \Theta_{\text{abs}}, \mu = 0) d\varepsilon - \int_{E_{g2}}^{\infty} N(\varepsilon, T_{\text{cell}}, \Theta_{\text{emit}}, \mu_2) d\varepsilon \right), \end{aligned} \quad (\text{B1})$$

where the coefficients $2/3$ and $1/3$, as explained for the ILCs, are the portion of transverse and longitudinal directions, respectively. The terms in first, second, and third large parentheses in the square brackets on the right-hand side of the above equation are the number of absorbed photons minus the number of emitted photons related to sub-band gap E_{g1} , sub-band gap E_{g2} , and band gap E_g , respectively, and the terms in the final large parentheses are related to the number of absorbed photons minus the number of emitted photons for the longitudinal direction. μ_T , μ_1 , and μ_2 are defined as

$$\begin{aligned}\mu_T &= E_{FC} - E_{FV} = qV, \\ \mu_1 &= E_{FC} - E_{F1} = qV - \mu_2, \\ \mu_2 &= E_{F1} - E_{FV} = qV - \mu_1.\end{aligned}\quad (\text{B2})$$

For each configuration of the fundamental band gap and sub-band gaps (E_g , E_{g1} , and E_{g2}), there is a voltage, referred to V_M , that maximizes $P_{\text{out}} = VJ(E_g, E_{g1}, E_{g2}, T_{\text{Sun}}, T_{\text{cell}}, \Theta_{\text{abs}}, \Theta_{\text{emit}}, V)$. It is calculated by evaluating the following partial differential equation:

$$\left(\frac{\partial P_{\text{out}}}{\partial V} \right)_{E_g, E_{g1}, E_{g2}} = 0. \quad (\text{B3})$$

It is worth mentioning that the FLE for each energy configuration of E_g , E_{g1} , and E_{g2} can be calculated with V_M and J_M (the current density at V_M) as

$$\begin{aligned}\eta_F &= \frac{(P_{\text{out}})_M}{P_{\text{in}}} \\ &= \frac{V_M J_M(E_g, E_{g1}, E_{g2}, T_{\text{Sun}}, T_{\text{cell}}, \Theta_{\text{abs}}, \Theta_{\text{emit}}, V_M)}{\int_0^\infty N(\varepsilon, T_{\text{Sun}}, \Theta_{\text{abs}}, \mu = 0) d\varepsilon}.\end{aligned}\quad (\text{B4})$$

- [1] W. Shockley and H. J. Queisser, Detailed balance limit of efficiency of p-n junction solar cells, *J. Appl. Phys.* **32**, 510 (1961).
- [2] G. Oh, Y. Kim, S. J. Lee, and E. K. Kim, Broadband antireflective coatings for high efficiency InGaP/GaAs/InGaAsP/InGaAs multi-junction solar cells, *Sol. Energy Mater. Sol. Cells* **207**, 110359 (2020).
- [3] F. Predan, O. Höhn, D. Lackner, A. Franke, H. Helmers, and F. Dimroth, Development and analysis of wafer-bonded four-junction solar cells based on antimonides With 42% efficiency under concentration, *IEEE J. Photovoltaics* **10**, 495 (2020).
- [4] M. H. Elshorbagy, E. López-Fraguas, F. A. Chaudhry, J. M. Sánchez-Pena, R. Vergaz, and B. García-Cámara, A monolithic nanostructured-perovskite/silicon tandem solar cell: Feasibility of light management through geometry and materials selection, *Sci. Rep.* **10**, 2271 (2020).
- [5] L. Hu, et al., Quantum-Dot tandem solar cells based on a solution-processed nanoparticle intermediate layer, *ACS Appl. Mater. Interfaces* **12**, 2313 (2020).
- [6] S. Asahi, K. Kusaki, Y. Harada, and T. Kita, Increasing conversion efficiency of two-step photon up-conversion solar cell with a voltage booster hetero-interface, *Sci. Rep.* **8**, 872 (2018).
- [7] W. Cai, Z. Zhang, Y. Jin, Y. Lv, L. Wang, K. Chen, and X. Zhou, Application of TiO₂ hollow microspheres incorporated with up-conversion NaYF₄:Yb³⁺, Er³⁺ nanoparticles and commercial available carbon counter electrodes in dye-sensitized solar cells, *Solar Energy* **188**, 441 (2019).
- [8] W. J. Ho, C. Y. Wei, J. J. Liu, W. C. Lin, and C. H. Ho, Performance characterization of planar silicon solar cells using NIR up-conversion layer comprising YF₃:Yb³⁺/Er³⁺ phosphors, *Vacuum* **166**, 1 (2019).
- [9] M. B. de la Mora, O. Amelines-Sarria, B. M. Monroy, C. D. Hernández-Pérez, and J. E. Lugo, Materials for down-conversion in solar cells: Perspectives and challenges, *Sol. Energy Mater. Sol. Cells* **165**, 59 (2017).
- [10] M. C. Beard, Multiple exciton generation in semiconductor quantum dots, *J. Phys. Chem. Lett.* **2**, 1282 (2011).
- [11] A. Green Martin, J. Keevers Mark, I. Thomas, B. Lasich John, K. Emery, and R. King Richard, 40% efficient sunlight to electricity conversion, *Prog. Photovoltaics Res. Appl.* **23**, 685 (2015).
- [12] D. Lan and M. A. Green, The potential and design principle for next-generation spectrum-splitting photovoltaics: Targeting 50% efficiency through built-in filters and generalization of concept, *Prog. Photovoltaics Res. Appl.* **27**, 899 (2019).
- [13] D. T. Nguyen, L. Lombez, F. Gibelli, S. Boyer-Richard, A. Le Corre, O. Durand, and J. F. Guillemoles, Quantitative experimental assessment of hot carrier-enhanced solar cells at room temperature, *Nature Energy* **3**, 236 (2018).
- [14] G. Wang, et al., An internally photoemitted hot carrier solar cell based on organic-inorganic perovskite, *Nano Energy* **68**, 104383 (2020).
- [15] A. Luque and A. Martí, Increasing the Efficiency of Ideal Solar Cells by Photon Induced Transitions at Intermediate Levels, *Phys. Rev. Lett.* **78**, 5014 (1997).
- [16] M. L. Lee, F. W. Huang, P. C. Chen, and J. K. Sheu, Gan intermediate band solar cells with Mn-doped absorption layer, *Sci. Rep.* **8**, 8641 (2018).
- [17] D. Kim, S. Hatch, J. Wu, K. A. Sablon, P. Lam, P. Jurczak, M. Tang, W. P. Gillin, and H. Liu, Type-II InAs/GaAsSb quantum Dot solar cells With GaAs interlayer, *IEEE J. Photovoltaics* **741-745**, 741 (2018).
- [18] S. Asahi, T. Kaizu, and T. Kita, Adiabatic two-step photoexcitation effects in intermediate-band solar cells with quantum dot-in-well structure, *Sci. Rep.* **9**, 7859 (2019).
- [19] Y. Takeda, Intermediate-band effect in hot-carrier solar cells, *Prog. Photovoltaics Res. Appl.* **27**, 528 (2019).
- [20] H. Hosokawa, R. Tamaki, T. Sawada, A. Okonogi, H. Sato, Y. Ogomi, S. Hayase, Y. Okada, and T. Yano, Solution-processed intermediate-band solar cells with lead sulfide quantum dots and lead halide perovskites, *Nat. Commun.* **10**, 43 (2019).

- [21] T. Hidouri, M. Biswas, I. Mal, S. Nasr, S. Chakrabarti, D. P. Samajdar, and F. Saidi, Engineering of carrier localization in BGaAs SQW for novel intermediate band solar cells: Thermal annealing effect, *Solar Energy* **199**, 183 (2020).
- [22] M. M. Wilkins, E. C. Dumitrescu, and J. J. Krich, Material quality requirements for intermediate band solar cells, *IEEE J. Photovoltaics* **10**, 467 (2020). 8962356
- [23] Z. Arefinia, Modelling of intrinsic loss processes in the intermediate band solar cells, *Z. Naturforsch. A* **74**, 51 (2019).
- [24] Z. Arefinia and A. Asgari, Quantum engineering of intrinsic losses in the diluted nitride InAsN quantum dot intermediate band solar cell, *PHOTOE* **9**, 1 (2019).
- [25] S. Jenks and R. Gilmore, Quantum dot solar cell: Materials that produce two intermediate bands, *J. Renewable Sustainable Energy* **2**, 013111 (2010).
- [26] S. E. Jenks, Drexel University, 2012.
- [27] V. P. Kunets, C. S. Furrow, T. A. Morgan, Y. Hirono, M. E. Ware, V. G. Dorogan, Y. I. Mazur, V. P. Kunets, and G. J. Salamo, InGaAs quantum wire intermediate band solar cell, *Appl. Phys. Lett.* **101**, 041106 (2012).
- [28] V. P. Kunets, C. S. Furrow, M. E. Ware, L. D. De Souza, M. Benamara, M. Mortazavi, and G. J. Salamo, Band filling effects on temperature performance of intermediate band quantum wire solar cells, *J. Appl. Phys.* **116**, 083102 (2014).
- [29] M. Kovalova, S. Kondratenko, A. Yakovlev, C. Furrow, V. Kunets, M. Ware, and G. Salamo, in *Proceedings of SPIE - The International Society for Optical Engineering* (2015).
- [30] N. A. Al Saqri, et al., Investigation of electrically active defects in InGaAs quantum wire intermediate-band solar cells using deep-level transient spectroscopy technique, *Nanotechnology* **28**, 045707 (2017).
- [31] M. S. Kovalova, S. V. Kondratenko, C. S. Furrow, V. P. Kunets, M. E. Ware, and G. J. Salamo, in *Proceedings of SPIE - The International Society for Optical Engineering* (2014).
- [32] Z. Arefinia, in *27th Iranian Conference on Electrical Engineering (ICEE)* (2019), pp. 5.
- [33] Z. Arefinia and A. Asgari, A new modeling approach for graphene based silicon nanowire schottky junction solar cells, *J. Renewable Sustainable Energy* **6**, 043132 (2014).
- [34] Z. Arefinia and A. Asgari, Optical and electrical modeling of solar cells based on graphene/Si nanowires with radial p-i-n junctions, *Sol. Energy Mater. Sol. Cells* **137**, 146 (2015).
- [35] S. L. Chuang, *Physics of Photonic Devices* (John Wiley & Sons, Hoboken, New Jersey, United States, 2009).
- [36] S. Saravanan, A. John Peter, and C. W. Lee, Phonon effects on interband optical transitions in InAs_{0.8}P_{0.2}/InP quantum wire, *J. Lumin.* **169**, 86 (2016).
- [37] V. P. Kunets, et al., Interface roughness scattering in laterally coupled InGaAs quantum wires, *Appl. Phys. Lett.* **97**, 262103 (2010).
- [38] V. P. Kunets, S. Prosandeev, Y. I. Mazur, M. E. Ware, M. D. Teodoro, V. G. Dorogan, P. M. Lytvyn, and G. J. Salamo, Isotropic hall effect and “freeze-in” of carriers in the InGaAs self-assembled quantum wires, *J. Appl. Phys.* **110**, 083714 (2011).
- [39] M. Bokalič and M. Topič, *Spatially Resolved Characterization in Thin-Film Photovoltaics* (Springer International Publishing, New York City, United States, 2015).
- [40] A. Luque and S. Hegedus, *Handbook of Photovoltaic Science and Engineering* (Wiley, Hoboken, New Jersey, United States, 2011).
- [41] P. Würfel, *Physics of Solar Cells: From Principles to New Concepts* (Wiley, Hoboken, New Jersey, United States, 2008).
- [42] T. Fukushi, T. Muranaka, T. Kimura, and H. Hasegawa, in *16th IPRM. 2004 International Conference on Indium Phosphide and Related Materials* (2004), pp. 450.
- [43] D. Gustiono, E. Wibowo, and Z. Othaman, Synthesis and characterization of InGaAs nanowires grown by MOCVD, *J. Phys.: Conf. Ser.* **423**, 012047 (2013).
- [44] M. Yahyaoui, K. Sellami, K. Boujdaria, M. Chamarro, and C. Testelin, Band parameters of InGaAs/GaAs quantum dots: Electronic properties study, *Semicond. Sci. Technol.* **28**, 125018 (2013).
- [45] S.-H. Wei and A. Zunger, Calculated natural band offsets of all II–VI and III–V semiconductors: Chemical trends and the role of cation d orbitals, *Appl. Phys. Lett.* **72**, 2011 (1998).
- [46] J. Wu and Z. M. Wang, *Quantum Dot Solar Cells* (Springer, New York, 2013).
- [47] A. Tiutiunnyk, I. Pérez-Quintana, D. Laroze, C. A. Duque, and M. E. Mora-Ramos, Influence of conduction-band non-parabolicity on terahertz intersubband Raman gain in GaAs/InGaAs step asymmetric quantum wells, *Appl. Phys. A* **126**, 23 (2019).
- [48] J. C. Slater and G. F. Koster, Simplified LCAO method for the periodic potential problem, *Phys. Rev.* **94**, 1498 (1954).
- [49] A. Martí, L. Cuadra, and A. Luque, Partial filling of a quantum dot intermediate band for solar cells, *IEEE Trans. Electron Devices* **48**, 2394 (2001).
- [50] A. Luque and A. Martí, A metallic intermediate band high efficiency solar cell, *Prog. Photovoltaics Res. Appl.* **9**, 73 (2001).
- [51] R. Strandberg and T. W. Reenaas, Photofilling of intermediate bands, *J. Appl. Phys.* **105**, 124512 (2009).
- [52] J. Hwang, K. Lee, A. Teran, S. Forrest, J. D. Phillips, A. J. Martin, and J. Millunchick, Multiphoton Sub-Band-Gap Photoconductivity and Critical Transition Temperature in Type-II GaSb Quantum-Dot Intermediate-Band Solar Cells, *Phys. Rev. Appl.* **1**, 051003 (2014).
- [53] A. Luque, A. Martí, and L. Cuadra, Thermodynamic consistency of sub-bandgap absorbing solar cell proposals, *IEEE Trans. Electron Devices* **48**, 2118 (2001).
- [54] S. P. Bremner, R. Corkish, and C. B. Honsberg, Detailed balance efficiency limits with quasi-Fermi level variations [QW solar cell], *IEEE Trans. Electron Devices* **46**, 1932 (1999).
- [55] N. J. L. K. Davis, M. L. Böhm, M. Tabachnyk, F. Wisnivesky-Rocca-Rivarola, T. C. Jellicoe, C. Ducati, B. Ehrler, and N. C. Greenham, Multiple-exciton generation in lead selenide nanorod solar cells with external quantum efficiencies exceeding 120%, *Nat. Commun.* **6**, 8259 (2015).

- [56] F. E. Osterloh, Maximum theoretical efficiency limit of photovoltaic devices: Effect of band structure on excited state entropy, *J. Phys. Chem. Lett.* **5**, 3354 (2014).
- [57] L. C. Hirst and N. J. Ekins-Daukes, Fundamental losses in solar cells, *Prog. Photovoltaics Res. Appl.* **19**, 286 (2011).
- [58] O. Dupré, R. Vaillon, and M. A. Green, *Thermal Behavior of Photovoltaic Devices: Physics and Engineering* (Springer International Publishing, New York City, United States, 2016).
- [59] P. T. Landsberg and V. Badescu, Carnot factor in solar cell efficiencies, *J. Phys. D: Appl. Phys.* **33**, 3004 (2000).
- [60] R. A. Serway and J. W. Jewett, *Physics for Scientists and Engineers with Modern Physics* (Cengage Learning, Boston, Massachusetts, United States, 2013).
- [61] M. A. Green, E. D. Dunlop, J. Hohl-Ebinger, M. Yoshita, N. Kopidakis, and A. W. Y. Ho-Baillie, Solar cell efficiency tables (version 55), *Prog. Photovoltaics Res. Appl.* **28**, 3 (2020).
- [62] L. Zhu, K.-H. Lee, M. Yamaguchi, H. Akiyama, Y. Kanemitsu, K. Araki, and N. Kojima, Analysis of nonradiative recombination in quantum dot solar cells and materials, *Prog. Photovoltaics Res. Appl.* **27**, 971 (2019).
- [63] V. Deligiannakis, G. Ranepura, I. L. Kuskovsky, and M. C. Tamargo, Advanced material system for the design of an intermediate band solar cell: Type-II CdTe quantum dots in a ZnCdSe matrix, *J. Appl. Phys.* **126**, Y (2019).
- [64] P. Persson and G. Strang, A simple mesh generator in MATLAB, *SIAM Review* **46**, 329 (2004).
- [65] Y. A. Goldberg, M. P. Mikhailova, and S. Rumyantsev, *Handbook Series on Semiconductor Parameters - Volume 2: Ternary and Quaternary III-V Compounds* (World Scientific, Singapore, 1999).
- [66] C. P. Kuo, S. K. Vong, R. M. Cohen, and G. B. Stringfellow, Effect of mismatch strain on band gap in III-V semiconductors, *J. Appl. Phys.* **57**, 5428 (1985).